Shallow strained $In_xGa_{1-x}As/In_yGa_{1-y}As$ superlattices embedded in *p-i-n* diodes: Structural properties and optical response

F. Royo, R. Schwedler, and J. Camassel
G.E.S.-C.N.R.S., cc074-Université Montpellier 2, F-34095 Montpellier cedex 5, France

R. Meyer* and H. Hardtdegen
I.S.I., Forschungszentrum Jülich, D-52425 Jülich, Germany

B. Fraisse
L.A.M.M.I.-C.N.R.S., cc004-Université Montpellier 2, F-34095 Montpellier cedex 5, France

(Received 18 December 1995)

$In_{1-x}Ga_xAs/In_{1-y}Ga_yAs$ strained layer superlattices grown on InP substrates are interesting candidates for optoelectronic device applications. When embedded in the intrinsic region of a *p-i-n* diode, the optical properties of such shallow strained superlattice devices depend critically on the precise control of the layer parameters and the built-in electric field. In this work, we investigate in detail the structural and optical properties of a series of $In_{1-x}Ga_xAs/In_{1-y}Ga_yAs$ superlattices with nominally lattice-matched wells and up to 1.5% tensile strained barriers, embedded in the intrinsic region of InP *p-i-n* diodes. The structural parameters have been determined from a careful line-shape analysis of x-ray rocking curves. An accurate model of the field-dependent electronic states in the superlattices has been developed. We find that the analysis of absorption and emission experiments requires taking into account the electric field screening by the photoinduced carriers. For fields above a few kV/cm, the optical properties are dominated by the mixed type-I–type-II band structure of the strained superlattices. [S0163-1829(96)04520-9]

I. INTRODUCTION

Since the early proposal by Osbourn that $In_{1-x}Ga_xAs/In_{1-y}Ga_yAs$ strained layer superlattices (SLS's) deposited on InP wafers should be useful advanced electronic materials,[1] they have been extensively considered for optoelectronic device applications.[2–14] As a consequence, in the recent years, enhanced TM-mode gain lasers have been reported,[4] as well as polarization insensitive amplifiers.[5] In the particular class of $In_{1-x}Ga_xAs/In_{1-y}Ga_yAs$ superlattices (SL's) considered in this work ($x=0.47$, $y>0.47$), spatially indirect alignment of the light-hole valence band has also been demonstrated, allowing for electro-optic modulators based on the mixed type-I–type-II Wannier-Stark effect[6,12–15] (WSE) to be constructed. Altogether, this makes these strained microstructures and related shallow $In_{1-x}Ga_xAsP$-based heterostructures appealing candidates to design optoelectronic integrated circuits operating in the 1.55-μm range.

Shallow $In_{1-x}Ga_xAs/In_{1-y}Ga_yAs$ SL's are a particular and simple class of *constant-y* materials recently introduced by Mircea *et al.*[16,17] This concept, usually applied to $In_{1-x}Ga_xAs_yP_{1-y}$ quantum-well structures, avoids any gradient of the group V elements throughout the heterostructure. This approach results in an improved interface abruptness with respect to the more conventional $In_{1-x}Ga_xAs/InP$ system.[18,19] In addition to these growth related aspects, the device stability against postgrowth thermal treatment (e.g., annealing of contacts) is also an important aspect for device design. In shallow SL systems, the advantages of WSE devices can be obtained using relatively thick ($\geqslant 8$ nm) layers, which lead to an improved thermal stability.[20]

Despite this technical interest, little is known about the details of the optical properties of $In_{1-x}Ga_xAs/In_{1-y}Ga_yAs$ SL's embedded in the intrinsic part of a *p-i-n* junction. There are several reasons to explain this lack of information. First, for any serious analysis, there are four structural parameters (layer thicknesses and compositions of wells and barriers) to be accurately determined. For instance, the band discontinuities estimated for the shallow $In_{1-x}Ga_xAs/In_{1-y}Ga_yAs$ SL's are only of the order of 25–100 meV. They are highly sensitive even to small deviations in the layer parameters. Their precise determination is therefore crucial for any quantitative interpretation of the SL's confined states.

Second, because the width of the strained SL barriers has to be kept small in order to ensure that the lattice mismatch is totally accommodated by elastic strain, carrier delocalization effects have to be evaluated. For instance, at zero electric field, the delocalization would result in the formation of minibands (MB's) centered at the uncoupled ground-state energies,[21] while, in the presence of a large built-in electric field, one would employ a picture of partially localized electrons and holes, possibly spatially separated in different quantum wells. This is the so-called Wannier-Stark localization.[22–24]

In this paper, we present a detailed investigation of the structural, electronic, and optical properties of a series of unbiased $In_{1-x}Ga_xAs/In_{1-y}Ga_yAs$ *p-i-n* diodes embedded in InP. We demonstrate that the formation of MB's and the Wannier-Stark effect are crucial for both emission and absorption of light by shallow $In_{1-y}Ga_xAs/In_{1-y}Ga_yAs$ SL *p-i-n* diodes. In the Sec. II, we focus on the nominal design

of the samples and on details of the growth technology. In Sec. III we describe the experimental procedures used for optical spectroscopy and x-ray diffractrometry. We show that, using an analysis based on the kinematic approach, a precise determination of both composition and thickness of the wells and barriers is possible. Our findings are compared to results obtained using a standard five crystal diffractometer and analyzing the data in the framework of the dynamical model. Starting from the structure parameters obtained by x-ray diffractrometry, we calculate in Sec. IV, without any free parameters, theoretical interband transition energies. The calculations take into account both the mixed type-I–type-II band structure and the effect of the built-in electric field. We compare these results to data from low-temperature photoluminescence (PL) and transmission experiments in Sec. VI. We will finish this paper with some concluding remarks.

II. SAMPLE PREPARATION

The samples were grown in a commercial horizontal low-pressure metal-organic vapor phase epitaxy reactor equipped with a vent-run switching manifold.[25] The reactor was operated at a total gas pressure of 20 hPa, with a gas velocity of 2.8 m/s. The metal-organic and hydride sources were, respectively, trimethyl-gallium (TMGa), trimethyl-indium (TMIn), and PH_3 and AsH_3. When necessary, dimethyl-zinc (DMZn) and H_2S were used as dopant sources.

To ensure a good compositional control of the SL layers, two pairs of TMGa and TMIn sources have been used for growth of the lattice-matched and Ga-rich $In_{1-x}Ga_xAs$ layers, respectively. During a growth run, two different values of the III/V ratios have been used, depending on the material being deposited. For all $In_{1-x}Ga_xAs$-type material, we have used a constant III/V ratio of 125. For the InP-type material, a much larger value (475) was selected. In both cases, the growth temperature was 640 °C. These conditions resulted in a typical growth rate of about 1 μm/h. Growth interruption sequences have been performed at each interface. They lasted for 5 and 3 s, respectively, when changing from InP to $In_{1-x}Ga_xAs$ and vice versa. When growing the SL's, growth interruptions of 3 s under arsine were performed.

Three samples (corresponding to runs 1061, 1062, and 1064, respectively) will be considered. They consisted in *p-i-n*-diodes (Fig. 1) grown on highly *n*-type doped ⟨100⟩ InP substrates. The SL's were embedded in the intrinsic region of the devices. They were made of 10 $In_{1-x}Ga_xAs$ wells nominally lattice matched to InP ($x=0.47$) separated by 11 Ga-rich, tensile strained, $In_{1-x}Ga_xAs$ ($x\approx0.58$) barriers. From run to run, the only intentional change concerned the well thickness (see Table I). On both sides of the SL's, two large (400 nm thickness) nonintentionally doped InP barriers were deposited. These intrinsic layers of the structure were embedded in two layers of *p*-type InP (200 nm) and *n*-type InP (100 nm), respectively, to form the *p-i-n* devices. To allow for an independent check of the barrier composition, a thin (30 nm) topmost Ga-rich $In_xGa_{1-x}As$ layer was deposited using the barrier growth conditions. This layer was *p*-type doped to a level of $p\approx10^{18}$ cm^{-3}.

The value of the built-in electric field was estimated from the nominal sample layout (Table I and Fig. 1) and later

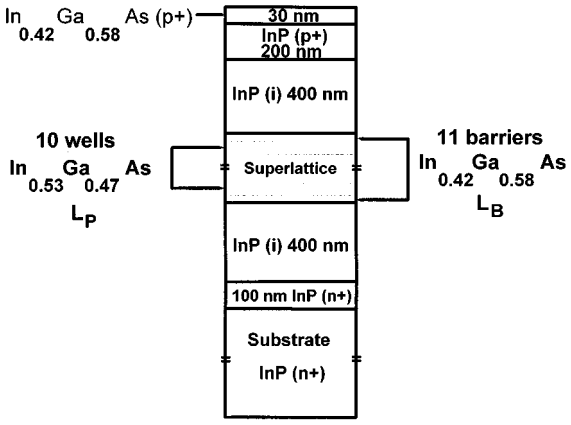

FIG. 1. Schematic of the structure of the $In_{1-x}Ga_xAs/In_{1-y}Ga_yAs$ SL *p-i-n* diodes. The nominal layer parameters of the SL's investigated are summarized in Table I.

corrected slightly using the structural parameters obtained from x-ray diffractrometry. Assuming that no background doping is present in the SL, and that dopant diffusion into the undoped layers at growth time is negligible, we obtain built-in electric fields in the range of 15 ± 1 kV/cm for all samples. Of course, the precise value depends slightly on the different period lengths of the three samples, but the interesting result is that, during the optical inspection of the samples, part of the estimated electric field can be screened by the photogenerated carriers. This screening effect will be discussed in detail in Sec. VI.

III. EXPERIMENT

A. Optical details

For photoluminescence (PL) and optical transmission (TR) spectroscopies, the samples were mounted in a liquid-He cryostat kept at 2 K. Luminescence was excited by 50 mW of 488 nm Ar-laser radiation focused to about 0.4 mm (excitation density 50 W/cm^2). Alternatively, the sample could also be irradiated by using 6 mW of 632 nm HeNe-laser radiation (excitation density 5 W/cm^2). For the transmission experiments, the light source was a tungsten-halogen lamp. In this case, the total excitation density was about 5 mW/cm^2 focused on a spot of 1-mm diameter. In every case, the optical signal was dispersed using a 0.75-m grating monochromator and detected using a cooled *p-i-n* germanium photodiode and conventional lock-in techniques.

B. X-ray diffraction

We have used two different diffractometers for the analysis of the $In_{1-x}Ga_xAs/In_{1-y}Ga_yAs$ SL's. First, systematic experiments were conducted on every piece of sample using a home-made two-crystal diffractometer equipped with a Cu anticathode. The GaSb monochromator allowed us to collect ⟨004⟩ diffractograms. In this case, a simulation software based on a kinematical approach[26–28] was used to analyze the diffractograms. This approach, with related theoretical background, will be discussed in detail in Sec. III C.

Second, we have used a horizontal high-resolution five-crystal x-ray diffractometer for verification of the results ob-

TABLE I. Summary of layer widths and compositions obtained for the series of samples investigated in this work. For each structural parameter, the table contains the nominal value, the result obtained by x-ray analysis within the dynamical model, and the corresponding result obtained by the kinematic model. Where applicable, the relative deviations are also indicated. The deviations are discussed in the text.

Sample	SL period Å	InGaAs cap layer		InGaAs barriers		InGaAs wells	
		x (Ga)	L_C (Å)	x (Ga)	L_B (Å)	x (Ga)	L_W (Å)
1061							
Nominal	155	0.58	300	0.58	70	0.47	85
Dynamic	144 (−7 %)	0.57	260 (−13 %)	0.57	66	0.467	78
Kinematic	144 (−7 %)	0.571	250 (−17 %)	0.571	60	0.473	84
1062							
Nominal	200	0.58	300	0.58	70	0.47	130
Dynamic	187 (−7 %)			0.567	66	0.47	121
Kinematic	187 (−7 %)	0.566	250 (−17 %)	0.566	75	0.464	112
1064							
Nominal	220	0.58	300	0.58	70	0.47	150
Dynamic	203 (−8 %)	0.567	260 (−13 %)	0.567	66	0.468	137
Kinematic	203 (−8 %)	0.568	250 (−17 %)	0.568	81	0.467	122

tained with the more simple setup. In this case, the Ge monochromator was set in the ⟨220⟩ mode and ⟨004⟩ diffractograms were collected on the central piece of the wafer. They were analyzed using standard simulations based on the dynamical diffraction theory.[29] As usual, given a model structure, the software solves the Tagaki-Taupin equations[30,31] and displays a theoretical line shape that has to be compared to the experimental one in order to optimize the final value of the parameters.

C. Kinematic approach to x-ray diffractograms

As already said, $In_xGa_{1-x}As/In_yGa_{1-y}As$ SL's are very shallow-band offset systems in which all unwanted modifications of the SL parameters modify strongly the optical response of the processed devices. This is the reason that all structural parameters have to be carefully checked on every piece of sample by x-ray diffractrometry. Because this systematically involves fitting the x-ray diffractograms, care must be taken to avoid any ambiguity that might be induced by the fitting procedure.

The kinematic approach used here to analyze the x-ray diffractograms is based on the procedure outlined by Quillec *et al.*[7] In this framework, the diffracted x-ray intensity for a finite superlattice of N periods of width P can be written as

$$I(u)=N^2\sum_k \sum_{k'} |C^1_{kk'}+C^2_{kk'}|^2 \mathrm{sinc}\left[\pi NP\left(u-\frac{k}{P}\right)\right], \quad (1)$$

where

$$C^i_{kk'}=\frac{Z_i}{a_i}\mathrm{sinc}\left[\pi Z_i\left(\frac{k}{P}-\frac{k'}{a_i}\right)\right] \quad (2)$$

and

$$\mathrm{sinc}(x)=\sin(x)/x. \quad (3)$$

The spatial frequency u is related to the diffraction angle via a standard Bragg relation, k is the order of diffraction of the SL peak, and k' the order of diffraction of the substrate material ($k'=4$ in this study); a_i and Z_i represent the lattice constants in the growth direction and the thicknesses of the individual layers, respectively.

The diffractograms consist of two sets of diffraction peaks associated with the individual layers (Fig. 2). The corresponding envelope functions (described by the $C^i_{kk'}$) are peaked at k'/a_i. The thicknesses of both the wells and barriers can be derived from the width of the envelope functions. The diffractograms are further modulated due to the last term in Eq. (1). This periodic series of peaks allows one to obtain the SL period $P=a_1+a_2$, directly, with a very high high precision.

When the lattice constants of the wells and barriers are sufficiently different, the envelope functions are well separated and can be fitted separately.[7] In this case, however, the kinematic approach has proven sufficient to deduce all structural parameters from the diffractograms.[7,9,15]

The situation is more complicated when the strain is not compensated and when the SL is very shallow. In this case, the envelope functions originating from the wells and barri-

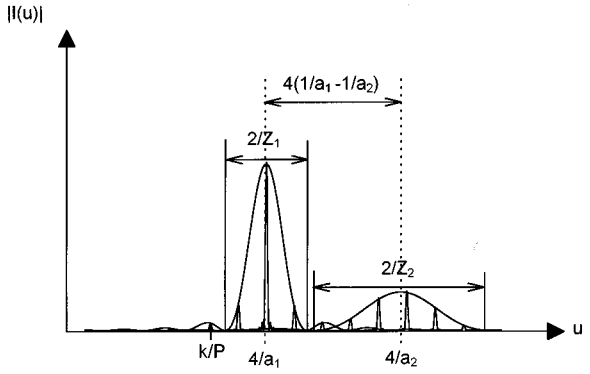

FIG. 2. Schematic representation of the x-ray diffractograms of a strained superlattice. The a_i denote the lattice parameters, the Z_i represent the layer thicknesses ($P=Z_1+Z_2$), and k is the order of the diffraction peak.

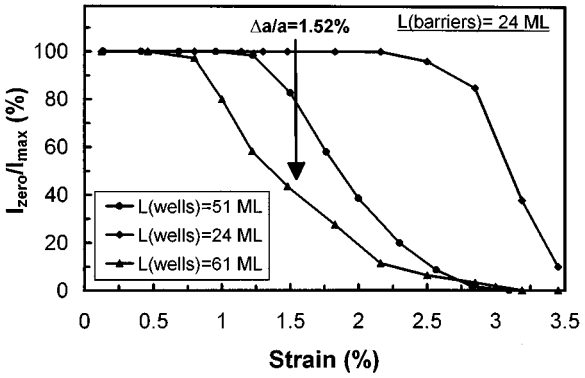

FIG. 3. The calculated intensity of the *zero-order* x-ray diffraction peak of a $In_{1-x}Ga_xAs/In_{0.53}Ga_{0.47}As$ superlattice with fixed barrier width in dependence of the barrier strain for several well widths. The layer thicknesses are indicated in the figure.

ers overlap, and the evaluation of the individual layer thicknesses and compositions is not at all straightforward.

Moreover, the so-called zero-order superlattice peak that is most commonly used to determine the average lattice constant in nearly lattice-matched samples, and corresponds to a value of $k=k_0$ for which $k_0/a_1+k_0/a_2$ is close to k', is no longer the strongest superlattice peak. If substantial net strain is present in the structure, it might even be very small. This is shown in Fig. 3. We display for different values of the layer parameters the relative change in intensity of the zero-order peak versus strain. Figure 3 demonstrates clearly that for reasonable barrier strain, the peak intensity may be quite low, making a simple identification of the zero-order peak impossible. In these cases a full line-shape analysis is necessary to obtain the average lattice constant.

Both the standard commercial software, which provides a full dynamical simulation of the x-ray rocking curves,[25] as well as the kinematic model described here[10,11] have been used previously in this situation. In any case, an independent method to verify the layer parameters obtained by the x-ray analysis is needed. In this work, we have used the transition energies obtained by optical transmission and photoluminescence spectroscopies to perform this cross check.

IV. CALCULATION OF OPTICAL TRANSITIONS

The comparison of the x-ray results with optical spectra has been done by calculating the optical transition energies deduced from the structural parameters obtained by diffractometry without any free parameter. The calculations of the SL's confined states are performed in the framework of the envelope function theory,[21,32] taking into account the built-in electric field of the otherwise unbiased *p-i-n* diodes. Material parameters are interpolated from the binary values. Wherever possible, the bowing has been taken into account by using the well-known parameters of $In_{1-x}Ga_xAs$ lattice matched to InP. The parameters used here are taken from Refs. 33–39. Reference 39 also contains a thorough description of the transfer matrix formalism used to determine the SL's confined states, optical transition energies, and oscillator strengths. The verification of the important band-offset parameters for the $In_{1-x}Ga_xAs/In_{1-y}Ga_yAs$ SLs is discussed in Ref. 13.

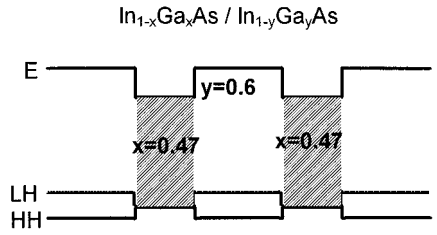

FIG. 4. Band lineup of $In_{0.53}Ga_{0.47}As/In_{0.40}Ga_{0.60}As$ demonstrating the mixed type-I–type-II band alignment.

A peculiar feature of $In_{0.53}Ga_{0.47}As/In_{1-x}Ga_xAs$ heterostructures is the mixed type-I–type-II valence band lineup (Fig. 4). In this case, the highest valence-band maximum in tensile strained $In_{1-x}Ga_xAs$ ($x>0.47$) is formed by the light-hole valence band, for which the strain-induced splitting of the normally degenerated $|3/2;3/2\rangle$ and $|3/2;1/2\rangle$ valence bands in bulk materials compensates the composition-induced change of the $In_{1-x}Ga_xAs$ band gap.[40,41,2] Then, for $x>0.47$, the light-hole band edge is raised above the light-hole band edge of lattice-matched $In_{0.53}Ga_{0.47}As$.[13] Therefore, in $In_{0.53}Ga_{0.47}As/In_{1-x}Ga_xAs$ heterostructures, carrier-type-dependent confinement occurs, as illustrated in Fig. 4. The light holes are confined to the Ga-rich layers while the electrons and heavy-hole states are confined to the lattice-matched layers.

The results of our computation are summarized in Fig. 5 (solid lines) for the case of type-I electron–heavy-hole transitions of sample 1062. Here, the transitions have been calculated for electric fields from 0 to 10 kV/cm. Three points should be outlined.

(i) In the absence of electric field, the calculations for the complete SL (23 layers, including the InP barriers) yield a MB of 10-meV width for the type I transitions. This is indicated by an arrow in Fig. 5. The corresponding wave functions are symmetric with respect to the complete SL structure. Therefore, the usual parity selection rules for carrier

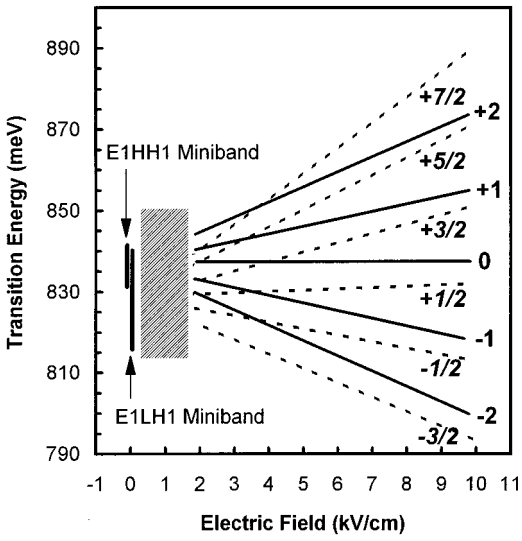

FIG. 5. Calculated optical transitions depending on electric field for sample 1062 ($T=2$ K).

wave functions in quantum wells apply.

(ii) For electric fields larger than 2 kV/cm, a reasonable localization of wave functions starts to occur. It develops more and more with increasing field and finally results in five localized Wannier-Stark states [commonly labeled E1HH1(0), E1HH1(± 1), and E1HH1(± 2)].

(iii) In between, neither Wannier-Stark localization nor delocalization does occur. This intermediate range requires analysis of *all* wave functions and transitions to understand the shape of the spectra (shaded area in Fig. 5).

In the WSE regime, the largest wave-function overlap, and therefore the largest oscillator strength, is always obtained for the $N=0$ transition between electron- and heavy-hole wave functions localized in the same well. The $N=\pm 1$ Wannier-Stark transitions are also present, but their intensity is weaker by at least a factor of four compared with the $N=0$ transitions. While these transitions are observable, it should be much more difficult to observe the even weaker $N=\pm 2$ ladders at any field.

Concerning the electron-light-hole transitions, the field-dependent variation has a more complicated structure. In contrast to the heavy-hole states, the light holes exhibit a strong delocalization due to their much smaller effective mass. As a consequence, because the confinement of the light holes is even smaller than that one of the electrons, the corresponding miniband at zero field is very large. When the electric field increases, a partial localization of the light-hole wave functions occurs but, in contrast to the electron wave functions, the light-hole states never get fully localized in a single superlattice layer. This behavior is a direct consequence of the shallowness of these superlattices. The appearance of the light-hole states is always in between the zero-field miniband picture and the Wannier-Stark picture. At any field, the light-hole states can be described by the center energy of their minibands rather than by a Wannier-Stark state energy. The centers of the corresponding optical transition energies have been displayed in Fig. 5 (dashed lines) but, opposite to the case of heavy holes (full lines), for any full interpretation, one has to keep in mind that the light-hole transitions in Fig. 5 represent the center of rather broad absorptions bands rather than a well-defined Wannier-Stark transitions.

V. STRUCTURAL ANALYSIS

The diffractogram obtained from sample 1064 with the two-crystal diffractometer is shown in Fig. 6(a). Five SL satellites (138–142) can be observed directly in addition to the InP substrate peak. The intensities of these satellites, and of some weaker ones, which are visible in the data after appropriate magnification, are summarized in Table II. Similar data have been collected on the three wafers and, from the angular spacing of the SL's structures, we deduced the experimental periods listed in Table I. Comparing with the expected (nominal) values, they appear systematically reduced by, typically, 7%. This clearly indicates a slightly overestimated growth rate for the average $In_{1-x}Ga_xAs$ material.

In Fig. 6(a), a broadband feature (marked by an asterisk) appears also around 32.1°. It comes from the top layer of Ga-rich $In_{1-y}Ga_yAs$ incorporated in all samples of the series and allows one to deduce the composition of the cap

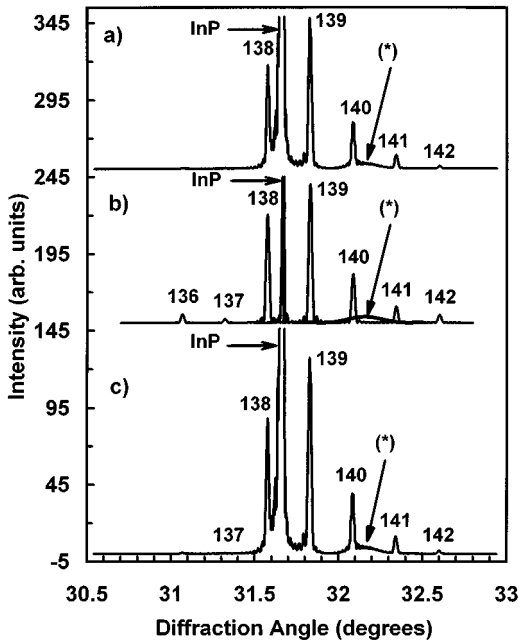

FIG. 6. (a) x-ray diffractogram obtained from sample 1064 using the two-crystal diffractrometer with (b) theoretical fit using the kinematic model. The numbers denote the SL diffraction orders. The structure indicated by an asterisk is due to the strained $In_{1-x}Ga_xAs$ top layer and further explained in the text. For comparison, the diffractogram obtained using the 5-crystal diffractometer is shown in (c).

layer, which, from the growth conditions, should be identical to that of the strained SL's barriers. Typical results of this fitting procedure are shown in Fig. 6(b). All resulting thicknesses and compositions of the cap layers have been listed in Table I.

While the compositions of the cap layers, which should equal the composition of the SL barriers, agree well (within 2%) with the targeted values, we find again that the cap layer thicknesses are lower than the nominal ones (see Table I). This confirms the overestimated growth rate for $In_xGa_{1-x}As$ deduced from the analysis of the total SL's pe-

TABLE II. Comparison of experimental x-ray SL peak intensities for sample 1064 (see Fig. 6) obtained using both diffractometers with the theoretical fits.

	I/I_{max}			
	Experiment		Theory	
SL order	5-crystal diffractometer	2-crystal diffractometer	Dynamic	Kinematic
135	0.2		0.2	
136	1.2	1.6	0.9	7.0
137	0.9	1.2	0.6	0.8
138	69.1	80.4	46	73
139	100	100	100	100
140	31.2	34.5	31.3	30.9
141	9.4	9.3	8.7	11.5
142	2.0	2.4	2	8.7
143	0.2			

riod. However, the discrepancy of the individual cap layer thicknesses from their design values is larger than that of the average $In_{1-x}Ga_xAs$ (see Table I), which suggests an imperfect calibration of the two different lines used for the growth of the respective material.

At this stage, the individual layer thicknesses and the composition of the nominally lattice matched layers remain the parameters to be fixed. Starting from the nominal values, they have to be slightly adjusted to give a reasonable agreement of experimental and theoretical diffracted intensities (see Table I).

A typical result, including the final comparison of experiment and simulation for sample 1064, is shown in Fig. 6(b). The agreement is rather satisfactory. However, some uncertainty arises due to the fact that it is not possible to fit simultaneously all peak intensities (see Table II) with high precision.

One may suspect that increasing the signal-to-noise ratio of the diffractograms, and thus the number of detectable superlattice peaks, could improve the precision of the procedure outlined here. To check this assumption, we collected x-ray diffractograms using a commercial Philips 5-crystal diffractrometer and the standard software provided with the instrument. The diffractogram obtained from sample 1064 is shown in Fig. 6(c).

While the better signal-to-noise ratio of the diffractogram in Fig. 6(c) allows observation of at least 11 superlattice peaks, qualitatively similar results were found. We followed the same protocol for the fit to the diffractogram of Fig. 6(c) (and also the diffractograms obtained from samples 1061 and 1062). Again we deduced the barrier composition from the topmost Ga-rich $In_xGa_{1-x}As$ layer and adjusted all remaining parameters slightly around their nominal value. The result of this fit in the kinematic model is displayed for all samples in Table I.

Comparing the results obtained by the analysis of both series of diffractograms, we find, for all samples, a very good agreement for the fitted layer compositions. From this result, we estimate an error of $\Delta x = 0.001$ for the layer compositions obtained by diffractrometry. This result is quite important concerning the evaluation of optical transition energies, as a variation by 1% causes a substantial band-gap variation of about 10 meV.

The results obtained for the thicknesses of the well and barrier layers exhibit much larger variations. While the period length can be determined with a precision of 1 Å , the determination of the individual layer thicknesses allows one to vary both without changing much the resulting fit. An error of ± 5 Å in these layer thicknesses therefore results. Fortunately, in the case of shallow superlattices investigated here, these errors have negligible influence on the computed transition energies.

VI. CHARACTERIZATION OF OPTICAL RESPONSE BY PHOTOLUMINESCENCE AND TRANSMISSION SPECTROSCOPY

Since we know the structural parameters with a reasonable accuracy, we can discuss the luminescence and absorption spectra in the energy range of the SL's band gaps. We know also that the SL's contain a built-in field of the order of 15 kV/cm (Sec. II), but for any optical experiment, part of this built-in electric field might be screened by the photogenerated carriers. Therefore, for every spectrum, the electrical field has to be determined self-consistently from the measurements.

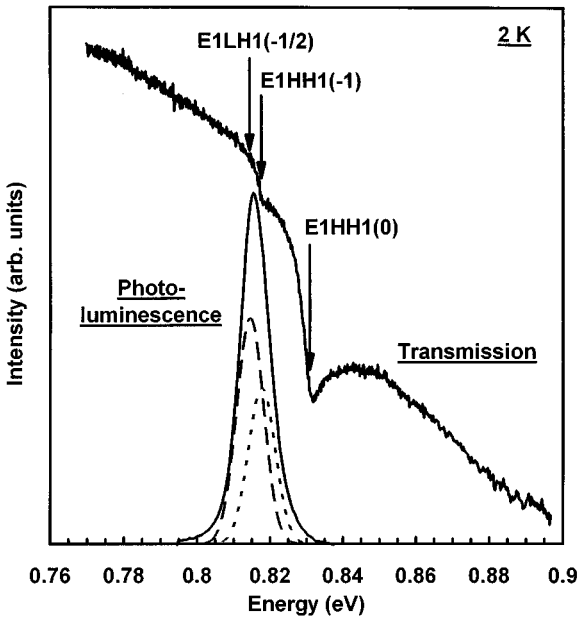

FIG. 7. Luminescence and optical transmission spectra of sample 1062 taken at $T = 2$ K. The fit to the PL spectrum is also shown.

PL and TR spectra from sample 1062 collected at 2 K are displayed in Fig. 7. The transmission spectrum exhibits two absorption edges of different strength, located at 818 and 831 meV, respectively. The high-energy transition displays a marked excitonic enhancement. The PL spectrum consists of a single broad band centered at 815 meV, with a weak shoulder around 820 meV. A line-shape analysis (also displayed in Fig. 7) reveals the presence of a second additional transition at 818 meV. This feature coincides with the weaker absorption edge.

To interpret the various optical transitions observed in PL and transmission in terms of the Wannier-Stark ladders estimated from our theoretical model (see Sec. IV), we have to come back to the oscillator strengths. As already said, from the overlap of two electron and hole wave functions localized in the same well [E1HH1(0) transition] and in two neighboring wells [E1HH(± 1) transitions] we estimated the *relative* oscillator strengths to be in the ratio of 1 to 4. This is just the same ratio of absorption structures found at 831 and 818 meV. As a consequence, we assign the main absorption peak observed in transmission at 831 meV to the strongest step in the joint density of states, i.e., the E1HH1(0) Wannier-Stark transition between electrons and heavy holes localized in the same layer. A nice point to notice is that, taking into account a reasonable excitonic binding energy of 4.5 meV for this transition, the transition energy is consistent with our model calculation using the structural parameters obtained from the x-ray analysis. This observation shows that the compositions and layer thicknesses obtained from the x-ray analysis are very reliable.

The lower energy transition (818 meV) originates from the E1HH1(-1) WS ladder. However, from the E1HH1(0) $-$ E1HH1(-1) energy splitting, which can be compared directly to the splitting depicted in Fig. 5, we estimate an electric field of only 9 kV/cm in the *p-i-n* diode. This value is much lower than the nominal one (15 kV/cm). We associate this deviation to a screening of part of the built-in electric field due to the illumination of the sample.

While producing the strong PL line, the type II transitions ($N=\pm 1/2$) show up very weakly on the transmission spectrum. We expected this behavior from our model calculations, since substantial broadening of the light-hole transitions was found (see Sec. IV). This broadening does not influence the observation of the PL peak, since PL is always enhanced for low-energy transitions due to the energy relaxation effect, but can explain the lack of a sharp transmission edge.

VII. CONCLUSION

Comparatively evaluating a series of $In_{0.53}Ga_{0.47}As/In_{1-x}Ga_xAs$ SLSs grown by low-pressure metal-organic chemical vapor deposition and using both x-ray and optical techniques, we have found that from the point of view of x-ray analysis, using in this case a simple kinematic approximation or a more complex dynamical model does not make a significant difference. In both cases, we obtain similar values for the series of SLS's well and barrier thicknesses and compositions; it is rather more important to adopt the line-shape fitting procedure to the particularities of the shallow superlattice system than to use a more elaborate theory.

Computing from these raw x-ray data the electronic energy levels, we found Wannier-Stark transition energies in good quantitative agreement with the experimental (optical) ones. The type-II transitions are characterized by transition energies that have to be explained by fractional Wannier-Stark indices ($\pm 1/2$, $\pm 3/2$) and by the lack of field-independent transition.[42,18]

For superlattices subject to an built-in electric field, we find that the most important low-temperature PL line corresponds to the energetic position of the $N=-1/2$ electron to light-hole Wannier-Stark transition. On the other hand, from the transmission experiments, we resolve mainly the $N=0$ and the $N=-1$ electron to heavy hole Wannier-Stark transitions. In any case, part of the electric field is found to be screened. The field therefore has to be determined carefully for each experimental situation.

ACKNOWLEDGMENT

One of the authors (R.S.) acknowledges support from the Alfred Kastler Foundation, Strasbourg, France.

*Present address: Universität Gesamthochschule Kassel, Fakultät für Elektrotechnik, Fachgebiet 16 (Technische Elektronik), 34132 Kassel, Germany.

[1] G. C. Osbourn, Phys. Rev. B **27**, 5126 (1983).
[2] J. E. Zucker, C. H. Joyner, and A. G. Dentai, IEEE Phot. Technol. Lett. **4**, 432 (1992).
[3] K. Magari *et al.*, IEEE Phot. Technol. Lett. **2**, 556 (1990).
[4] M. Okamoto *et al.*, IEEE J. Quantum Electron. **27**, 1463 (1991).
[5] K. Magari, M. Okamoto, and Y. Noguchi, IEEE Phot. Technol. Lett. **3**, 998 (1991).
[6] R. Schwedler *et al.*, J. Phys. (France) IV **3**, C5-445 (1993).
[7] M. Quillec *et al.*, J. Appl. Phys. **55**, 2904 (1984).
[8] A. Godefroy *et al.*, *Proceedings of the International Conference on InP and Related Materials* (Sociéte des Electriciens et des Electroniciens, IEEE Lasers and Electro-Optics Society, and IEEE Electron Devices Society, Paris, 1993), pp. 143–146.
[9] M. Quillec *et al.*, J. Appl. Phys. **59**, 2447 (1986).
[10] A. Kohl *et al.*, Mater. Sci. Eng. B **21**, 244 (1993).
[11] F. Royo *et al.*, Superlatt. Microstruct. **15**, 2 (1994).
[12] R. Schwedler *et al.*, Appl. Phys. A **57**, 199 (1993).
[13] R. Schwedler *et al.*, Phys. Rev. B **52**, 12 108 (1995).
[14] R. Schwedler *et al.*, Superlatt. Microstruct. **15**, 145 (1994).
[15] F. Royo *et al.*, *Semiconductor Heteroepitaxy—Growth, Characterization and Device Applications* (World Scientific, Singapore, 1995), pp. 502–505.
[16] A. Mircea, A. Ougazzaden, G. Primot, and C. Kazmierski, J. Cryst. Growth **124**, 737 (1992).
[17] A. Mircea *et al.*, *Proceedings of the 5th International Conference on Indium Phosphide and Related Materials* (IEEE, Paris, 1993).
[18] X. S. Jiang, A. R. Clawson, and P. K. L. Yu, J. Cryst. Growth **124**, 547 (1992).
[19] C. Rigo *et al.*, J. Cryst. Growth **136**, 293 (1994).
[20] J. Camassel, H. Peyre, and R. W. Glew, Mater. Sci. Eng. B **28**, 353 (1994).
[21] G. Bastard, *Wave Mechanics Applied to Semiconductor Heterostructures* (Editions de Physique, Paris, 1988).
[22] J. Bleuse, G. Bastard, and P. Voisin, Phys. Rev. B **60**, 220 (1988).
[23] J. Bleuse, P. Voisin, M. Allovon, and M. Quillec, Appl. Phys. Lett. **53**, 2632 (1988).
[24] P. Voisin *et al.*, Phys. Rev. B **61**, 1639 (1989).
[25] R. Meyer *et al.*, J. Cryst. Growth **124**, 583 (1992).
[26] V. S. Speriosu and J. T. Vreeland, J. Appl. Phys. **56**, 1591 (1984).
[27] J. M. Vandenberg, J. C. Bean, R. A. Hamm, and R. Hull, Appl. Phys. Lett. **52**, 1152 (1988).
[28] J. M. Vandenberg, M. B. Panish, H. Temkin, and R. A. Hamm, Appl. Phys. Lett. **53**, 1920 (1988).
[29] W. J. Bartels, J. Hornstra, and D. J. W. Lobeek, Acta Crystallogr. Sec. A **42**, 539 (1986).
[30] S. Tagaki, Acta Crystallogr. **15**, 1131 (1962).
[31] D. Taupin, Bull. Soc. Franç. Miner. Crist. **87**, 469 (1964).
[32] G. Bastard, Phys. Rev. B **24**, 5693 (1981).
[33] S. Adachi, J. Appl. Phys. **53**, 8775 (1982).
[34] D. Gershoni, H. Temkin, and H. B. Panish, Phys. Rev. B **38**, 7870 (1989).
[35] D. Gershoni, H. Temkin, H. B. Panish, and R. A. Hamm, Phys. Rev. B **39**, 5531 (1989).
[36] E. P. O'Reilly, Semicond. Sci. Technol. **4**, 121 (1989).
[37] C. V. de Walle, Phys. Rev. B **62**, 2028 (1989).
[38] K. H. Goetz *et al.*, J. Appl. Phys. **54**, 4543 (1983).
[39] S. Juillaguet *et al.*, in *Non-Stoichiometry in Semiconductors*, edited by K. J. Bachmann, H.-L. Hwang, and C. Schwab (North-Holland, Amsterdam, 1992), pp. 155–160.
[40] G. C. Osbourn, Phys. Rev. B **27**, 5126 (1983).
[41] M. Okamoto *et al.*, IEEE J. Quantum Electron. **27**, 1463 (1991).
[42] M. K. Saker *et al.*, Phys. Rev. B **43**, 4945 (1991).